ASTROBIOLOGY
Volume 14, Number 9, 2014

DOI: 10.1089/ast.2014.1165

Geology and Photometric Variation of Solar System Bodies with Minor Atmospheres: Implications for Solid Exoplanets

Yuka Fujii,[1] Jun Kimura,[1] James Dohm,[2] and Makiko Ohtake[3]

Abstract

A reasonable basis for future astronomical investigations of exoplanets lies in our best knowledge of the planets and satellites in the Solar System. Solar System bodies exhibit a wide variety of surface environments, even including potential habitable conditions beyond Earth, and it is essential to know how they can be characterized from outside the Solar System. In this study, we provide an overview of geological features of major Solar System solid bodies with minor atmospheres (*i.e.*, the terrestrial Moon, Mercury, the Galilean moons, and Mars) that affect surface albedo at local to global scale, and we survey how they influence point-source photometry in the UV/visible/near IR (*i.e.*, the reflection-dominant range). We simulate them based on recent mapping products and also compile observed light curves where available. We show a 5–50% peak-to-trough variation amplitude in one spin rotation associated with various geological processes including heterogeneous surface compositions due to igneous activities, interaction with surrounding energetic particles, and distribution of grained materials. Some indications of these processes are provided by the amplitude and wavelength dependence of variation in combinations of the time-averaged spectra. We also estimate the photometric precision needed to detect their spin rotation rates through periodogram analysis. Our survey illustrates realistic possibilities for inferring the detailed properties of solid exoplanets with future direct imaging observations. Key Words: Planetary environments—Planetary geology—Solar System—Extrasolar terrestrial planets. Astrobiology 14, 753–768.

1. Introduction

DIRECT IMAGING of rocky planets is expected to play an essential role in looking for signatures of life and investigating the surface environments of exoplanets. To develop our ability to decipher the light from unknown exoplanets, one possible starting point is to understand the photometric and spectroscopic features of well-known Solar System planets and satellites as if they were extrasolar bodies. For this purpose, Earth, among others, has been of significant interest in terms of habitability, and its disk-integrated spectrum has been studied both observationally (*e.g.*, Arnold *et al.*, 2002; Woolf *et al.*, 2002; Hamdani *et al.*, 2006; Turnbull *et al.*, 2006; Livengood *et al.*, 2011) and theoretically (*e.g.*, Ford *et al.*, 2001; Des Marais *et al.*, 2002; Tinetti *et al.*, 2006a, 2006b; Kaltenegger *et al.*, 2010; Robinson, 2011; Robinson *et al.*, 2011). Spectra of the Earth at different evolutionary stages have also been modeled by changing the bioactivity (Kaltenegger *et al.*, 2007; Sanromá *et al.*, 2013) and continental distribution (Sanromá and Pallé, 2012).

The appearance of other Solar System bodies also needs to be considered[1] as more general samples of exoplanets beyond Earth, because they are the only samples of planets whose real nature can be known in detail. In reality, various geological processes alter the surface reflectance of Solar System solid bodies at local to global scale, and they provide clues to the current conditions and evolution histories on which planetary habitability relies. Therefore, it is important to examine the detectability of their surface signatures from a distance. In the context of future applications to exoplanets, spectra of Solar System bodies have been

[1]We use the word ''body'' to refer to a planet or a moon without distinguishing them.

[1]Earth-Life Science Institute, Tokyo Institute of Technology, Tokyo, Japan.
[2]The University Museum, The University of Tokyo, Tokyo, Japan.
[3]Institute of Space and Astronautical Science, Japan Aerospace Exploration Agency, Kanagawa, Japan.

compiled, and characterization based on color-color plots has been discussed (Traub, 2003; Lundock *et al.*, 2009; Crow *et al.*, 2011). Mallama (2009) proposed the characterization of terrestrial exoplanets through orbital phase curves based on the empirical phase curves of Solar System planets. Hu *et al.* (2012) studied spectroscopic signatures of theoretical planets with various surface compositions inspired by Solar System bodies and put forward several observable features including Si-O features in the mid IR, an Fe band around 1 μm, and O-H bands in the near IR (NIR).

Along with these properties, time variability due to spin rotation could provide complementary information about surface geology. In the case of Earth, disk-averaged scattered light exhibits diurnal variation coherent with the change in the composition in the illuminated and visible region. Because the continental distribution is highly inhomogeneous, and the global cloud pattern does not change significantly in a day, the spin rotation period may be successfully identified through periodogram analysis (Pallé *et al.*, 2008), which then may allow for recovery of surface inhomogeneity along the equator (Cowan and Agol, 2008; Cowan *et al.*, 2009, 2011; Oakley and Cash, 2009; Fujii *et al.*, 2010, 2011, 2013) as well as estimation of the surface composition (Cowan and Strait, 2013).

In this study, we surveyed photometric variations of Solar System bodies with minor atmosphere and their relationship to surface geology by performing simulations based on the latest mapping products and by adopting the observed data of multiband photometry. In particular, the terrestrial Moon, Mercury, the Galilean moons, and Mars are considered[2]. Our intent was to study the general causes of photometric variation, estimate variation amplitude, and explore the possibility of identifying geological features as well as the spin rotation periods. After reviewing our current understandings of the surface colors and their relation to geological characteristics of Solar System bodies (Section 2), we describe our methods and data sets used to obtain multiband light curves for each body (Section 3). In Section 4, we present our main results, including simulated light curves, average spectra, and wavelength dependence of variation, and compare them with their characteristic geologies. The detectability of the spin rotation period is also examined in Section 4. In Section 5, we discuss the effects of atmospheres on photometric characterization; present another noteworthy example from the minor bodies in the Solar System, Iapetus; and offer a general caution on the interpretations of photometric properties. Our conclusions are summarized in Section 6.

2. Brief Review of the Surface Geological Features of Solar System Bodies with Minor Atmospheres

In this section, we provide an overview of the current understandings about the surface geologies of major Solar System solid bodies with minor atmospheres. We focus on features that influence planetary albedos in the UV/visible/NIR because they are parameters that are primarily accessible by future direct imaging observations of exoplanets.

In short, several major processes are identified as factors that vary planetary albedo regionally. These include compositional diversity due to igneous activities (*e.g.*, on Io and the terrestrial Moon), interactions between surface ice and surrounding plasma particles (on Europa, Ganymede, and Callisto), global tectonic deformation (*e.g.*, on Ganymede), and overlay of fine-grained materials (on Mars).

Below, we discuss the albedo characteristics of each body and their geological origins in detail.

2.1. Terrestrial moon

The terrestrial Moon is well known for the prominent dichotomy in its surface albedo. Bright areas (highlands) are predominantly made of anorthosite, which was deposited from a magma ocean in the very early stage of lunar history (Taylor, 1982; Warren, 1990). On the other hand, the dark areas (maria) are large impact basins that were filled with mafic basaltic lavas through volcanic activity in the later stage (the estimated age of mare basalt ranges from $\sim$4 to 1.5 Ga; Morota *et al.*, 2011). The greatest extent of maria is on the near side (Earth-facing hemisphere) (Wilhelms *et al.*, 1987), leaving the far side brighter. This hemispheric asymmetry is likely related to the difference in crustal thickness between the near and far sides; an equipotential surface is closer to the surface of the near side, and thus, magmas that originate at the same level can reach the surface more easily than on the far side (*e.g.*, Hiesinger and Head, 2006). Although the origin of the dichotomy in crustal thickness is still controversial, one convincing hypothesis is that it is due to massive impact events (Cadogan, 1981; Whitaker, 1981; Nakamura *et al.*, 2012). Typical examples of the reflectance spectra of highland and mare are shown in Fig. 1a. They exhibit a remarkable contrast in amplitude.

2.2. Mercury

Mercury exhibits relatively homogeneous gray color and is known to be covered with basaltic materials with common sulfur- and magnesium-rich characteristics (Nittler *et al.*, 2011, Rhodes *et al.*, 2011). At a closer look, there are both smooth plains and heavily cratered regions. Smooth plains, composing 40% of the surface, are thought to be volcanic plains erupted through fractured crust contemporaneous with the period of Late Heavy Bombardment (4.1–3.8 Ga)[3], while the heavily cratered regions indicate ancient crust. The color contrast among different geological units is much less obvious than that for the lunar surface partly because the colors of the volcanic deposits are brighter than their lunar counterparts (*i.e.*, mare basalt) due to the lower amount of iron (Lucey *et al.*, 2006; Nittler *et al.*, 2011; Rhodes *et al.*, 2011). In addition, geological activity on Mercury has been apparently dormant since the Late Heavy Bombardment, leaving a large percentage of the surface ancient ($>$3.8 Ga) (Strom, 1979) and saturated with impact

[2]We include Mars, although containing a minor atmosphere of $\sim$7.5 mbar, which influences its appearance; the surface of Mars is directly observable except during dust storms, compared to the cloud (haze)-shrouded Venus and Titan with surface colors completely obscured.

[3]The Late Heavy Bombardment, also referred to as the lunar cataclysm, is a putative event thought to have occurred approximately 4.1–3.8 Ga during which a large number of impact craters may have formed on the Moon and on other terrestrial planets.

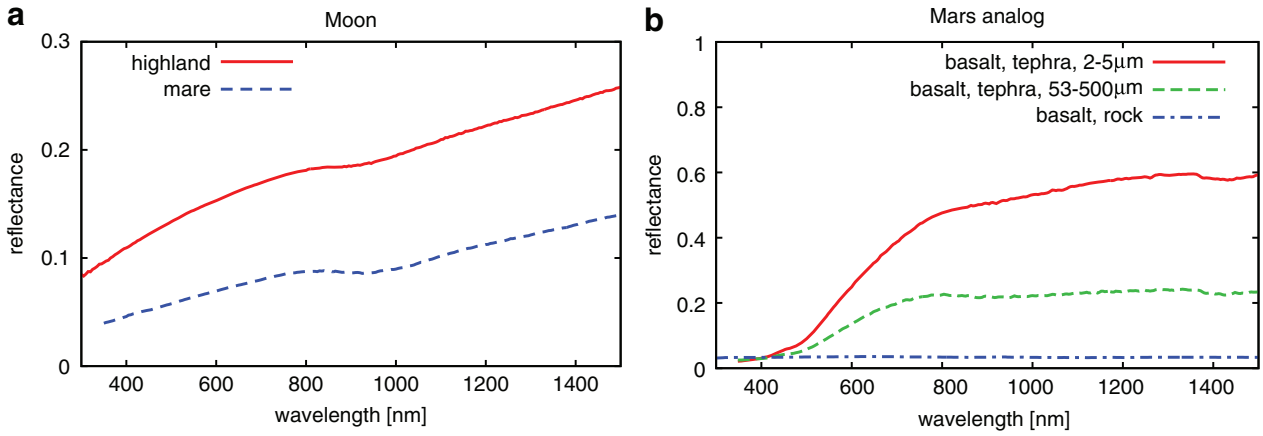

FIG. 1. (**a**) Reflectance spectra of two distinctive terrains, highland and mare, taken from the RELAB database (http://www.planetary.brown.edu/relab). Samples are ''62231 highland'' and ''12070 mare'' for highland and mare, respectively. (**b**) Reflectance spectra of simulants of the martian surface rock, taken from the PDS Geosciences Spectral Library (http://speclib.rsl.wustl.edu/search.aspx). The data sets adopted are those entitled ''Basalt; tephra/ash; altered; palagonite'' with varying particle sizes (Morris *et al.*, 2000, 2001). Color images available online at www.liebertonline.com/ast

craters; without geological activity, the long-lasting impact cratering process can deform old terrains and mix the volcanic materials (*e.g.*, Arvidson *et al.*, 1975; Schultz, 1989), which may have resulted in the relatively homogeneous color of Mercury's surface.

2.3. Galilean moons

The Galilean moons (Io, Europa, Ganymede, and Callisto) are the four largest moons that orbit Jupiter in synchronous rotation states (*i.e.*, for each body, the spin rotation period and orbital period coincide), implying one side permanently faces the planet, and a permanent ''leading'' and ''trailing'' hemisphere with respect to the orbital plane. The surface geologies of the Galilean moons are strongly affected by tidal forces due to the gravitational interaction with Jupiter as well as the interaction with surrounding plasmas that are produced through the acceleration of Io-derived particles by the fast-rotating jovian magnetosphere.

All the moons orbiting Jupiter, except Io, have icy surfaces. While surfaces covered with new, pure, and fine H_2O particles are typically bright and the albedo can reach close to 1, the actual geometric albedos of Europa, Ganymede, and Callisto are $\sim$0.7 (Moore *et al.*, 2004), $\sim$0.4 (Morrison and Morrison, 1977), and $\sim$0.2 (Moore *et al.*, 2004), respectively. Surface darkening likely originates from the following two processes. First, the longer the icy surface is exposed to space, the more it is contaminated by meteoritic materials; hydrated non-ice materials are generally dark and exhibit weak UV Fe^{3+} absorption and a positive visible-to-NIR slope, similar to some carbonaceous chondrites (space weathering) (Clark, 1980). Second, the annealing of ice results in larger grains and, hence, a darker surface (Johnson, 1997). In turn, brighter icy surfaces are generally younger, indicating the presence of dynamical activities such as plumes (*e.g.*, Porco *et al.*, 2006) and/or cryovolcanism (*e.g.*, Pappalardo *et al.*, 1998). Because these activities can be maintained by internal heat sources and the consequent mobility of the interior, the brighter surfaces may suggest the possibility of subsurface liquid layers, which could provide a potential habitat for extraterrestrial life.

A common albedo feature among Europa, Ganymede, and Callisto is the contrast between the leading and trailing hemispheres (*e.g.*, Stebbins and Jacobsen, 1928; Harris, 1961; Johnson, 1971; Blanco and Catalano, 1974; Morrison *et al.*, 1974; Millis and Thompson, 1975; Nash and Johnson, 1979). This pattern has been discussed in relation to the fact that the energetic plasmas trapped in the jovian magnetosphere preferentially hit the trailing hemispheres, although the details of the interactions between the surfaces and energetic particles remain uncertain. The degree of the hemispheric albedo dichotomy depends on the effects of excavation of pristine ice by meteoroid impacts (more influential on leading hemispheres) and radiolytic darkening processes (more influential on trailing hemispheres). Similar processes would work on a synchronously rotating body surrounded by plasmas or other materials.

2.3.1. Io. The surface of Io, the innermost of the four Galilean moons, shows diverse visible colors, which are identified as various volcanic-related sulfur-containing materials, such as yellow (sulfur), brown (radiolytically decomposed sulfur chains, S_x), gray (SO_2 frost), and black (silicate pyroclastics) (Carlson *et al.*, 2007, and references therein). Indeed, Io has the most intense volcanic activity in the Solar System, and more than 150 active volcanoes have been confirmed and distributed across the globe. These activities are sustained by the strong tidal interaction with Jupiter through deformation and dissipated heat.

2.3.2. Europa. The surface of Europa is mostly covered with bright ice, as a consequence of the active resurfacing process maintained by internal heat sources; the age of Europa's surface is estimated at $\sim$20–180 Ma (Zahnle *et al.*, 2003). However, there is a broad, brownish area in the trailing hemisphere. This is likely due to hydrated sulfuric acid, which can be naturally produced from the radiolysis of Io-derived sulfurous material and surface H_2O (Carlson *et al.*, 2002).

In addition, Europa's surface shows global cracked and disrupted terrains with dark colors. The NIR mapping spectrometer on board the Galileo spacecraft has identified

some hydrated salt minerals (*e.g.*, magnesium, sodium sulfate, and/or carbonate) that are strongly associated with geological processes (McCord *et al.*, 1998). While most hydrated salts are colorless, radiolytic products of sulfate and possibly sulfide compounds—in particular polymeric sulfur (*e.g.*, S_4 and S_8)—serve as coloring agents.

2.3.3. Ganymede. The surface geology of Ganymede is classified into two units. Forty percent of the surface is old and dark ($\sim$4.0 Ga; Zahnle *et al.*, 2003), while the remaining 60% is relatively young and brighter ($\sim$2.0 Ga; Zahnle *et al.*, 2003). The younger and brighter regions contain evidence of global tectonic deformation such as extensive arrays of grooves and ridges. Currently, it is believed that the lithosphere is extensionally strained because of global expansion (Showman *et al.*, 1997) possibly caused by past internal heating events. In addition, Ganymede has polar caps (greater than $\sim$40°) that are likely composed of water frost and are noticeably brighter than the equatorial regions (Khurana *et al.*, 2007).

2.3.4. Callisto. The surface of Callisto is globally dark, probably due to long exposure to space without resurfacing. The age of Callisto's surface is estimated to be ancient ($\sim$4.0 Ga; Schenk *et al.*, 2004), with no evidence of tectonic activity, probably because the tidal force exerted on Callisto in its distant orbit from Jupiter is not enough to produce sufficient heat. Callisto also shows albedo contrast between leading and trailing hemispheres, but it depends on the geometric configuration between the Sun, Callisto, and the observer. Except for opposition phase, that is, at the configuration where the direction of the Sun and the observer coincide, the trailing hemisphere is brighter in visible light (*e.g.*, Moore *et al.*, 2004), unlike Europa and Ganymede. Near the opposition phase, the leading hemisphere is brightened up (''opposition surge'') more prominently than the trailing hemisphere, resulting in even reversed contrast, possibly because of the rougher, less compacted leading hemisphere due to the enhanced micrometeoritic erosion (*e.g.*, Buratti, 1995).

2.4. Mars

The martian surface exhibits a global red color due to iron oxides (''rust''), the origin of which is still controversial. Increasing evidence points to aqueous activities in the past (*e.g.*, Head *et al.*, 1999; McEwen *et al.*, 2007; Squyres *et al.*, 2012), which would have contributed to the formation of rust; rust forms when oxygen comes in long-term contact with iron.

In addition, the martian surface shows significant global variation in albedo. Although the origins of the albedo features are not fully understood, bright regions (typically with albedos larger than 0.2) are largely attributed to fine-grained materials (<10 μm; *e.g.*, Ruff and Christensen, 2002) (see Fig. 1b), which are mostly created by wind through mechanical weathering; in general, smaller particle size results in higher albedo (*e.g.*, Adams and Filice, 1967). Other contributing factors to the albedo signature likely include variations in rock composition affected by hydrological/geological activities through time (*e.g.*, Tharsis-driven transient flooding, ocean formation, and volcanism; Baker *et al.*, 1991, 2007; Dohm *et al.*, 2007, 2009). The albedo distribution pattern has not changed significantly over the past few decades, according to a comparison of the observations by Viking and the Mars Global Surveyor (MGS).

Another notable feature of the martian surface is the hemispheric dichotomy in surface elevation—the cratered highlands of the southern hemisphere and the lowlands of the northern hemisphere—the origin of which is still under debate (for details, see Dohm *et al.*, 2013, and references therein). In addition, the Tharsis volcanic bulge that dominates the western hemisphere (centered near the equator and $\sim$265 longitude) is also distinct (Carr and Head, 2010). These factors may also have affected the distribution of grained materials, while there does not appear to be an one-to-one relationship due to the complex interactions of geological, hydrologic, periglacial, glacial, gravity-driven, and eolian processes through time.

3. Method and Data Sets to Compile Rotational Color Variation

Motivated by the diversity in the planetary surfaces reviewed in Section 2, we studied the photometric properties of the Solar System bodies as if they were extrasolar objects (*i.e.*, as point sources), with a focus on the time variation according to spin rotation. We did so by running simulations of the disk-integrated light curves based on the pixel-level scattering properties of each body and by collecting the observed disk-integrated photometry of each body. We detail our methods below.

3.1. Simulations

We performed simulations of light curves by the following procedure (see also *e.g.*, Ford *et al.*, 2001; Fujii *et al.*, 2010). First, the relative configuration of the host star (*i.e.*, the Sun), body, and observer is fixed. We assume that the star and observer are in the equatorial plane of the body and that both the star and observer are distant (*i.e.*, the incident light and the scattered light are treated as parallel to the star-body line and body-observer line, respectively). Then, the configuration is specified by the star-body-observer angle (''phase angle'') α (left panel of Fig. 2).

Next, the surface of the body is pixelated into $2° \times 2°$ pixels. The incident zenith angle, θ_0, the zenith angle of observation, θ_1, and the relative azimuthal angle, ϕ, are computed for each pixel based on the relative configuration of the star and observer as well as the location of the pixel (right panel of Fig. 2). The scattering property of each surface pixel is represented by the bidirectional reflectance distribution function (BRDF), the ratio of the scattered radiance, $I(\theta_0, \theta_1, \phi)$, to the irradiance, F_0, $f(\theta_0, \theta_1, \phi; \mathbf{p}_{\vec{r}}) \equiv \frac{I(\theta_0, \theta_1, \phi)}{F_0}$. Here, $\vec{r}$ denotes the location of the pixel, and $\mathbf{p}_{\vec{r}}$ is the parameter set specifying the function whose values vary pixel to pixel.

Finally, the contribution from each surface pixel is calculated by using the BRDF with a computed geometric parameter, θ_0, θ_1, and ϕ, and then the contributions are summed up to obtain the total scattered intensity from the body, as seen as a point source. We neglect the effect of atmospheres.

The necessary information to perform the integral is the BRDF at each pixel, $f(\theta_0, \theta_1, \phi; \mathbf{p}_{\vec{r}})$. We approximately rewrite the BRDF as a product of the reflectance, $a_{\vec{r}}$, and the

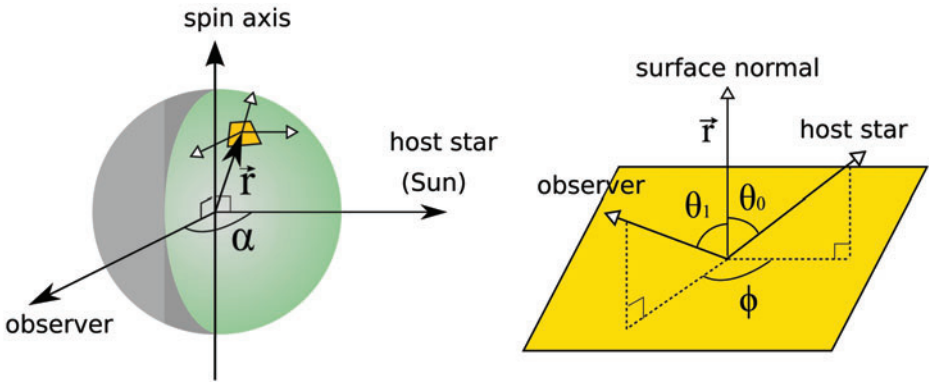

FIG. 2. Schematic configuration of star-planet (moon)-observer system. Color images available online at www.liebertonline.com/ast

function responsible for the anisotropy $\tilde{f}(\theta_0, \theta_1, \phi; \mathbf{p})$, that is, $f(\theta_0, \theta_1, \phi; \mathbf{p}_{\vec{r}}) = a_{\vec{r}}\tilde{f}(\theta_0, \theta_1, \phi; \mathbf{p}_{\vec{r}})$. Then, we assign values for $a_{\vec{r}}$ and $\mathbf{p}_{\vec{r}}$ based on the available mapping data sets. The data used in this paper are described below and summarized in Table 1. The examples of the reflectance maps are displayed in Figure 3.

For the terrestrial Moon, we obtain reflectance maps at the 414, 749, 901, 950, and 1000 nm bands derived with the Multi-band Imager (MI) on board the lunar orbiting spacecraft SELENE (Kato *et al.*, 2008) and use them to find $a_{\vec{r}}$ (Fig. 3). We adopt the same anisotropic function, $\tilde{f}(\theta_0, \theta_1, \phi; \mathbf{p})$, as the one used in the derivation of $a_{\vec{r}}$, which is a combination of the phase function and the lunar Lambert function (Eq. 11 of Yokota *et al.*, 2011). Since the function includes four parameters, $\mathbf{p}_{\vec{r}}$, which depend on the reflectance $a_{\vec{r}}$, we classify the surface into three categories (low/medium/high reflectance regions) based on $a_{\vec{r}}$ at $\lambda = 750$ nm, following Yokota *et al.* (2011), and assign corresponding $\mathbf{p}_{\vec{r}}$, depending on its category (Fig. 10 of Yokota *et al.*, 2011). The BRDF was obtained by Yokota *et al.* (2011) for $5° < \alpha < 85°$, $\theta_0 < 85°$, and small θ_1. Thus, when α or θ_0 is larger, we fix the BRDF value to that of $\alpha = 85°$ or $\theta_0 = 85°$, while extrapolating it in terms of θ_1. This admittedly inconsistent treatment may limit the validity of the model.

For Mercury, we used reflectance maps based on observations by the MESSENGER probe (Hawkins *et al.*, 2007; Domingue *et al.*, 2011a, Domingue *et al.*, 2011b) at 430, 480, 560, 630, 750, 830, 900, and 1000 nm for $a_{\vec{r}}$ (Fig. 3). We assumed the anisotropic function derived for Mercury in Domingue *et al.*, 2011a, which is based on Hapke model (*e.g.*, Hapke 1986).

For the Galilean moons, the map of Io based on Galileo/SSI observations (Belton *et al.*, 1992; Geissler *et al.*, 1999; Becker and Geissler, 2005) at 404, 559, and 756 nm was available and used for $a_{\vec{r}}$ (Fig. 3). For Europa, Ganymede, and Callisto, however, we were unable to obtain global reflectance maps at different bands; only grayscale maps were available (Becker *et al.*, 2001). The contrast in brightness that appears in the maps is the collection of observations at different photometric bands as well as postprocessing. Therefore, while we also performed simulations with those data accompanied by the Lambert law, those results are only for reference.

In the case of Mars, we used the data sets of bolometric albedo in the 300–2900 nm range obtained with MGS/TES (Christensen *et al.*, 2001) for $a_{\vec{r}}$ (Fig. 3). Consistently with Thermal Emission Spectrometer (TES) data processing, we assumed the Lambert law; $\tilde{f}(\theta_0, \theta_1, \phi; \mathbf{p}_{\vec{r}}) \equiv 1$.

3.2. Observed disk-integrated photometric data

We also checked the availability of the observed disk-integrated photometry of the bodies to be used in the study. While there are many observations of spatially unresolved images of Solar System bodies to date (for a comprehensive

Table 1. Data Sources of Global Albedo Maps

Target	*Source*	*Effective/Central wavelength (nm)*
Terrestrial Moon	SELENE/MI	414, 749, 901, 950, 1000
Mercury	MESSENGER/MDIS[1]	430, 480, 560, 630, 750, 830, 900, 1000
Io	Galileo/SSI[2]	404 (violet), 559 (green), 756 (NIR)
Europa, Ganymede, Callisto		
	Voyager[3]	280–640 (clear)
	Galileo/SSI[3]	611 (clear), 559 (green), 756 (NIR)
Mars	MGS/TES[4]	300–2900

[1]http://messenger.jhuapl.edu/the_mission/mosaics.html
[2]http://astrogeology.usgs.gov/search/details/Io/Voyager-Galileo/Io_Galileo_SSI_Global_Mosaic_ClrMerge_1km/cub
[3]*Europa:* http://astrogeology.usgs.gov/search/details/Europa/Voyager-Galileo/Europa_Voyager_GalileoSSI_global_mosaic_500m/cub. *Ganymede:* http://astrogeology.usgs.gov/search/details/Ganymede/Voyager-Galileo/Ganymede_Voyager_GalileoSSI_global_mosaic_1km/cub. *Callisto:* http://astrogeology.usgs.gov/search/details/Callisto/Voyager-Galileo/Callisto_Voyager_GalileoSSI_global_mosaic_1km/cub
[4]http://geo.pds.nasa.gov/missions/mgs/tesspecial.html

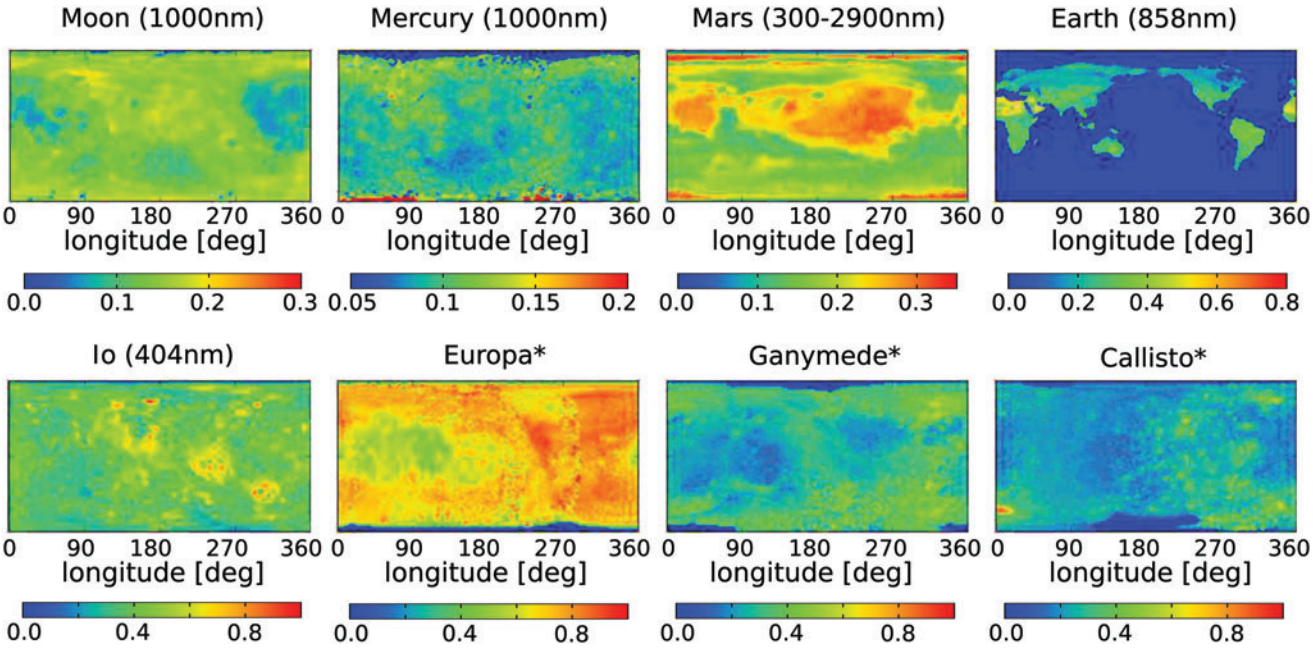

FIG. 3. Maps of planets and satellites considered in this paper, taken from the respective data sets listed in Table 1. All maps but those of Europa, Ganymede, and Callisto represent reflectance at the noted wavelengths. The data of Earth is based on MODIS BRDF/Albedo product (Schaaf *et al.*, 2002). Maps for Europa, Ganymede, and Callisto are grayscale images based on the compilation of observations from the Voyager and Galileo spacecrafts at different filters, and include significant processing. The longitude of the terrestrial Moon, Mercury, Mars, and Earth is indicated eastward from the prime meridian. The longitude of the Galilean moons is indicated eastward from the sub-jovian points; the left and right halves correspond to the trailing and leading hemispheres, respectively. Color images available online at www.liebertonline.com/ast

multiband photometry of Solar System planets, see, *e.g.*, Young and Irvine, 1967; Irvine *et al.*, 1968a, 1968b), it is not always straightforward to obtain data sets comparable to the observations from an astronomical distance because of the limitation of the observable configuration. In the following, we describe the data sets useful to examine photometric variability of each body where available.

First, it is difficult to obtain the spectra of the terrestrial Moon as if it were observed by a distant observer, because ground-based observations always involve the near side. Although far-side observations of the terrestrial Moon include those by Galileo's Solid-State Imaging (SSI) experiment (Belton *et al.*, 1992) and the Extrasolar Planet Observation and Characterization (EPOCh) mission (Crow *et al.*, 2011), as well as three images of the Earth-Moon system taken from afar by NASA's Voyager and Cassini, they are instantaneous snapshots that make it difficult to derive the color variation over the rotational period.

Observations of Mercury at various configurations also tend to encounter problems because of limitations in the observable geometry. While Mallama *et al.* (2002) conducted the photometry of Mercury at varying orbital and rotational phases by combining both space-based and ground-based observations, the precision was not sufficient to resolve the brightness variation along the equator.

Thus, we did not consider the observed data for the terrestrial Moon and Mercury but rather performed simulations based on the latest global maps as described above.

On the other hand, it is feasible to observe rotational variation (at near full phases) of outer bodies, including the Galilean moons and Mars, even from Earth. For the Galilean moons, we considered data sets from Millis and Thompson (1975; hereafter MT75) among the literature of ground-based observations of Galilean moons (*e.g.*, Stebbins and Jacobsen, 1928; Harris, 1961; Johnson, 1971; Blanco and Catalano, 1974; Morrison *et al.*, 1974; Nash and Johnson, 1979). We processed the observed UBV colors of Galilean moons listed in Tables II, III, IV, and V of MT75, following the procedure described in that paper. In particular, we obtained the photometric variation due to spin rotation at the phase angle $\alpha = 6°$ by correcting the phase angle dependence of the observed colors. For the purpose of comparison with other bodies, we interpreted the observed colors in terms of albedo (apparent albedo; see below) by comparing the observed magnitudes and the magnitude of a perfectly reflecting Lambert sphere with an identical radius.

For Mars, we obtained the data set of multiband photometry observed by the EPOCh mission with seven 100 nm wide filters ranging from 300 to 1000 nm (see also Crow *et al.*, 2011). The EPOCh Mars observations were conducted from November 20–21, 2009, and the phase angle was $\alpha = 37°$, corresponding to an illumination fraction of $\sim 90\%$. The subsolar and sub-observer latitudes are $\sim 5°$ and $\sim 15°$, respectively.

The observed data considered in this paper is summarized in Table 2.

4. Results

In this section, we present the light curves obtained by the procedure described in Section 3. After discussing the apparent features of each light curve (Section 4.1), we quantitatively

TABLE 2. DATA SOURCES FOR OBSERVED MULTIBAND PHOTOMETRY

Target	*Source*	*Effective/Central wavelength (nm)*
Galilean moons	Millis and Thompson (1975)	365 (U), 445 (B), 551 (V)
Mars	EPOCh[1]	350, 450, 550, 650, 750, 850, 950
Earth	EPOCh[1]	350, 450, 550, 650, 750, 850, 950

[1]PDS Small Bodies Node, http://pdssbn.astro.umd.edu/index.shtml

intercompare the averaged colors and their variability (Section 4.2) and examine the detectability of periodicity (Section 4.3).

We describe the reflectance of the bodies in terms of their apparent albedo, which is defined as the ratio of the scattered light flux from the planet divided by the flux that would be expected for a lossless Lambert sphere at the same phase (see also Qiu *et al.*, 2003; Cowan *et al.*, 2009). Note that the apparent albedo at the full phase is 1.5 times as large as the geometric albedo.

4.1. Light curves

The simulated light curves of the terrestrial Moon and Mercury are shown in Fig. 4. Here, the horizontal axis is the spin rotational phase angle in units of radians divided by 2π (*i.e.*, 1 corresponds to the configuration after one orbital period), starting at the point where the sub-observer point is at 0° (=360°) longitude; in Fig. 3, the sub-observer point moves from the right edge to the left edge. For the purpose of comparison with Mars, we fix the phase angle at $\alpha = 37°$. The snapshots shown at the bottom of each panel are based on the mapping products displayed in Fig. 3. The terrestrial Moon exhibits significant variation, with one peak and one trough corresponding to the dichotomy between hemispheres. In contrast, Mercury shows only small variations, with two enhancements around 0.25 and 0.75, corresponding to the two relatively bright regions around longitudes 270° and 90° shown in Fig. 3.

The modeled and observed rotational variation of the Galilean moons at $\alpha = 6°$, normalized so that the average is unity for display purposes, is shown in Fig. 5. The origin of the spin rotation phase in Fig. 5 is the superior conjunction,

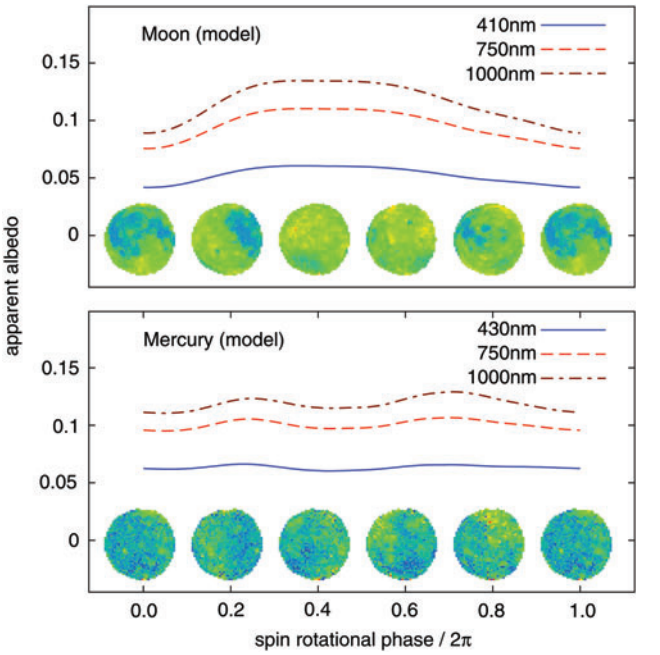

FIG. 4. Diurnal light curves of the terrestrial Moon and Mercury at full phase at different wavelengths. The snapshots at the bottom portray the surface reflectance maps at 1000 nm in the visible area (Fig. 3). Color images available online at www.liebertonline.com/ast

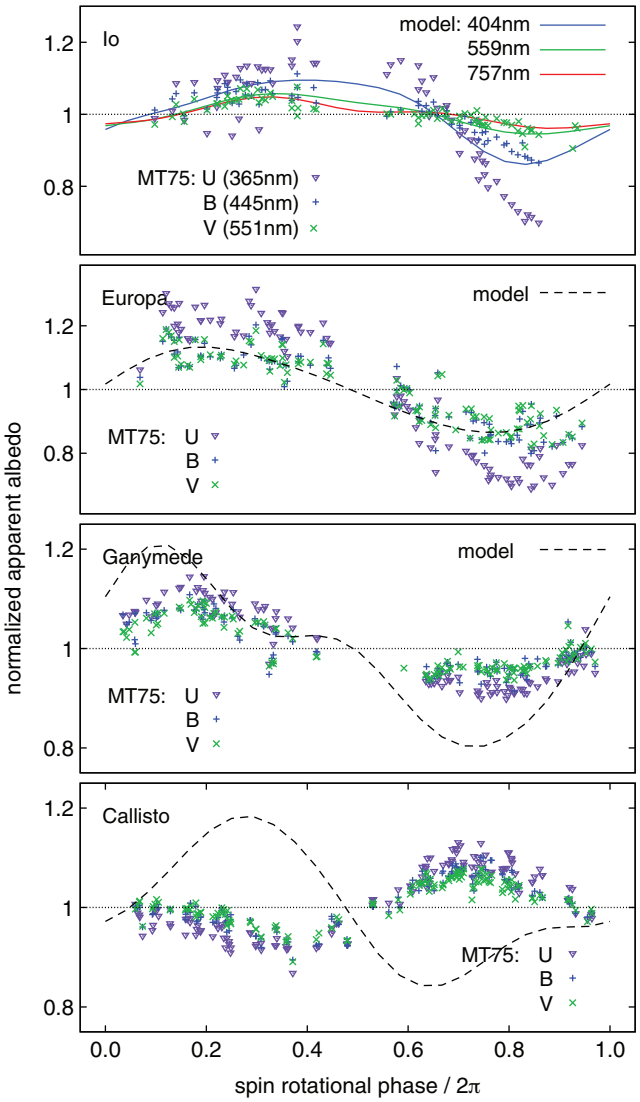

FIG. 5. Diurnal light curves of the Galilean moons. Normalized reflectance is plotted as a function of the spin rotational phase, with 0.0 being the phase where the sub-observer point is at the sub-jovian point. The leading and trailing hemispheres are observed at 0.25 and 0.75, respectively. Points are reduced from the UBV photometric observations of the Galilean moons by Millis and Thompson (1975). Solid and dashed lines are model light curves based on the global mapping data sets (Fig. 3); the lines for Europa, Ganymede, and Callisto are dashed to call attention to the apparent photometric inaccuracy of the input maps. Color images available online at www.liebertonline.com/ast

that is, the sub-observer point coincides with the sub-jovian point, which is 0° (=360°) longitude in Fig. 3; the sub-jovian point at phases 0.0–0.5 and 0.5–1.0 is in the leading and trailing hemispheres, respectively. The model and the observed data exhibit a consistent pattern. While the peak in the reflectivity around the rotational phase 0.2–0.6 can be attributed to the area of the surface covered with SO_2 frost at around 104–300° in longitude, the trough around phase 0.8 corresponds to the volcanic area covered with S (seen in orange or yellow in visible light) around 72° in longitude (Fig. 3). In reality, the reflectance of SO_2- and S-covered areas is the most different at $\lambda \sim 400$ nm, where S strongly absorbs the light due to the band gap (Clark, 1999), whereas SO_2 is reflective.

The primary feature of the light curves shared by Europa and Ganymede—the sinusoidal shape originating from the dichotomy between the bright leading and dark trailing hemispheres—has been reproduced by models. In the case of Ganymede, the albedo dichotomy between the new and old terrains also modulates the light curves as a secondary effect. However, minor features of modeled Ganymede light curves show inconsistency with the data. For Callisto, the trend in the simulated light curves is almost opposite to the observed photometric variation. These are probably related to the postprocessing of the input mapping data sets and the lack of the detailed BRDF models, which include the peculiar phase-angle dependence of the leading and trailing hemispheres (Section 2.3.4). Because of the insufficient consistency, we will not use these two simulated light curves in the later analysis in Section 4.3.

Figure 6 displays the simulated light curves of Mars together with the observed multiband light curves, showing a reasonable consistency; the peak corresponds to the epoch where the bright region around Tharsis (~265° longitude) dominates the illuminated and visible area. The variation is evident at longer wavelengths, while it is muted at short wavelengths, which is consistent with the negligible difference in reflectance between fine-grained materials and rocks (Fig. 1b).

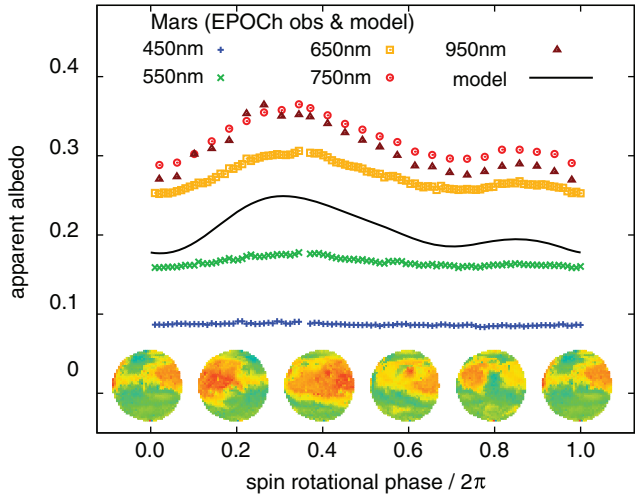

FIG. 6. Diurnal light curves of Mars at different wavelengths at phase 37°. The snapshots at the bottom are based on the MGS/TES bolometric albedo map (Fig. 3). Note that the subsolar and sub-observer latitudes in the observed data are ~5° and ~15°, respectively, while the model as well as snapshots assumes the observations from the equatorial plane for simplicity. Color images available online at www.liebertonline.com/ast

The variation patterns of the bodies considered here are coherent among different wavelengths. Consistently, principle component analysis on these light curves resulted in one dominant eigenspectrum with a proportion of variance larger than 99% (details not shown here). As the dimensionality of eigenvectors is, in theory, the number of the distinctive surface components minus 1 (Cowan *et al.*, 2011; Cowan and Strait, 2013), these results show no indication of the characteristic surface components more than 2.

The light curves at different orbital phase angles are different because of the narrower illuminating area and the effect of the BRDF. The effects of orbital phase angle are discussed in Section 4.3 below.

4.2. Average spectra and variability

Figure 7 summarizes the rotationally averaged spectra in the phases discussed in Section 4.1 and the peak-to-trough fractional variation at each of the wavelengths (we hereafter discuss the time variability in terms of fractional variation amplitude, which is defined as the peak-to-trough amplitude divided by the average, unless otherwise noted). The data on the Galilean moons here are based on MT75 after binning the data points over 30°. Just for reference, we also plotted the data of Earth at $\alpha = 58°$, obtained by EPOCh (Livengood *et al.*, 2011).

While all the atmosphereless bodies show ''red'' colors, the wavelength-dependent variation clearly indicates the diversity of surface materials. The bodies considered here exhibit 5–50% peak-to-trough variation amplitudes, depending on the wavelengths. Those that show large amplitudes are the terrestrial Moon, Io, and Europa, whereas Mercury, Ganymede, and Callisto all show small variations. The former group consists of bodies with relatively recent geological activities—formation of maria on the terrestrial Moon (compared to the more ancient cratered highlands), volcanism on Io, resurfacing on Europa—and thus may be identified as geologically interesting targets. On the other hand, members of the latter group commonly have ancient surfaces, where long-time exposure to space has resulted in muted signatures through impact mixing and space weathering.

In terms of the wavelength dependences, the variability of the terrestrial Moon and Mercury is mostly independent of wavelengths. On the other hand, Mars shows large variation only at longer wavelengths, because at longer wavelengths the relatively efficient scattering by fine-grained materials is noticeable, while at short wavelengths global existence of iron oxides absorbs light.

In contrast to these bodies, the Galilean moons, in particular Io and Europa, show strong variability at short wavelengths. The variability of Io at short wavelengths likely originates from the contrast between polymeric sulfur, which strongly absorbs light at $\lambda \sim 400$ nm, and surrounding reflective frost. For the three icy bodies, the non-uniformity of the degree of interactions with surrounding plasmas and space weathering plays a major role in the variability at short wavelengths (Section 2.3).

In general, both average spectra and their variability change according to the phase angles, because of changes in

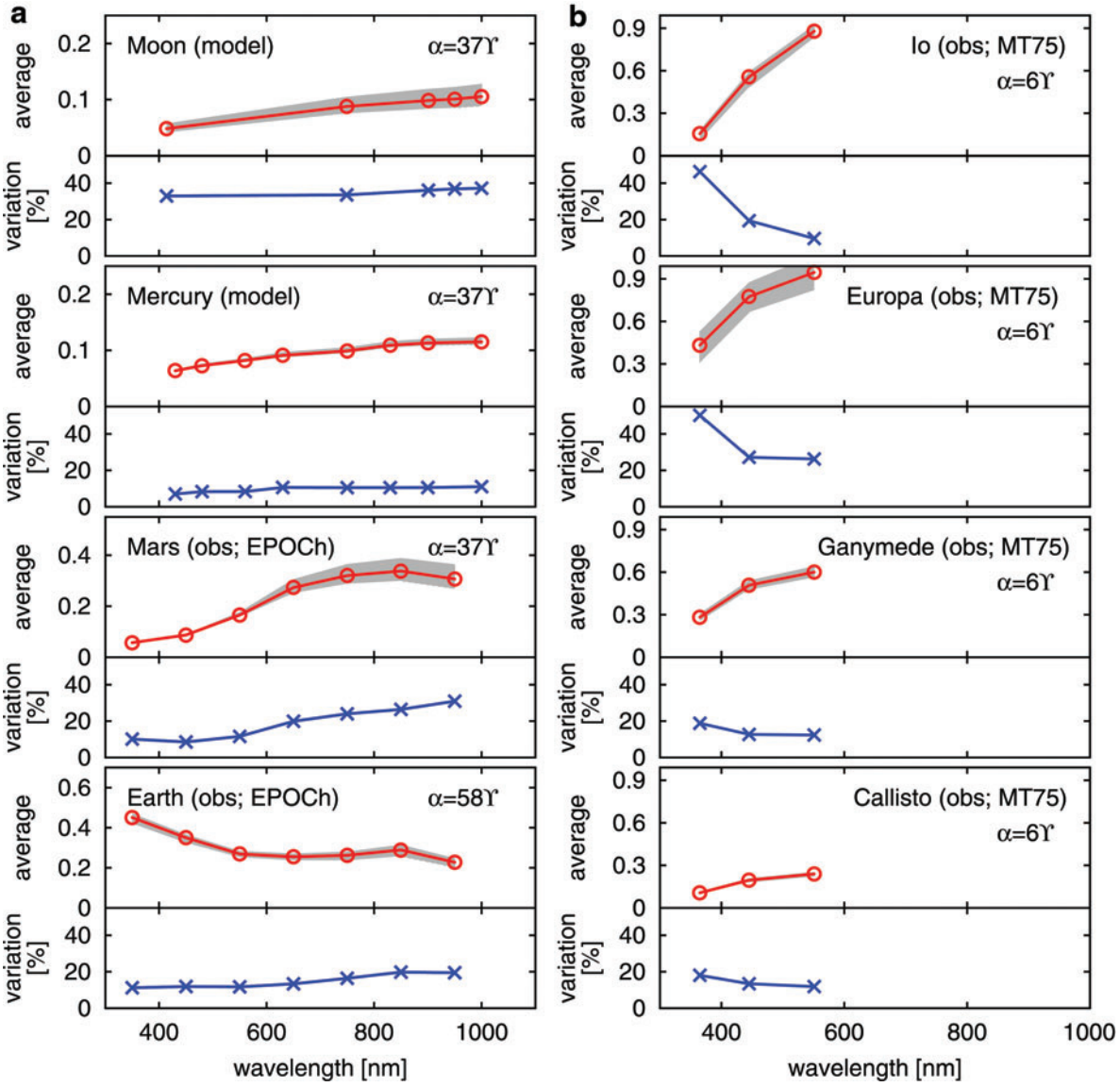

FIG. 7. Red: rotationally averaged low-resolution spectra of Solar System solid bodies. The shadowed regions show the peak-to-trough variation amplitude in one rotation. Blue: variation fraction spectra, defined as the peak-to-trough variation amplitude divided by the averaged spectra. Color images available online at www.liebertonline.com/ast

the area of the illuminated and visible region, and the anisotropic nature of surface scattering (BRDF). In our model, the fractional variation amplitudes of the terrestrial Moon at $\alpha = 6°$, 45°, and 90° are 35%, 40%, and 44%, respectively (see Section 4.3 and Fig. 8 below).

4.3. Detectability of spin rotation period

Based on the rotational variability of the bodies, we discuss the detectability of the spin rotation period though periodogram analysis. The determination of the planetary rotation period is important for at least two reasons. First, it is one of the parameters that enable us to assess the planet formation theory by comparing theoretical predictions (*e.g.*, Kokubo and Ida, 2007; Kokubo and Genda, 2010). The spin rotation period may also undergo later evolution by, for example, the presence of satellites. Second, knowing the planetary rotation period is necessary for phase folding the light curves, which could eventually allow us to map the surface and to take a closer look at localized geological features (Cowan *et al.*, 2009, 2011; Oakley and Cash, 2009; Fujii *et al.*, 2010, 2011, 2013; Kawahara and Fujii, 2010, 2011; Fujii and Kawahara, 2012).

The observational precision necessary for spin period measurement is roughly expected to be inversely proportional to the variation amplitude; to detect the periodicity of a sinusoid with amplitude A, observational noise would be roughly a few times smaller than A. To see more clearly, we estimate the signal-to-noise ratio (S/N) needed to detect the periodicity by the following procedure. The S/N here is defined by the ratio of planetary flux at each exposure (data point) to the standard deviation of the observational noise associated with each data point.

Given each theoretical (*i.e.*, noiseless) light curve, mock data sets are created by adding artificial Gaussian noises with varying S/N. Subsequently, we perform Lomb-Scargle periodogram analysis (Lomb, 1976; Scargle, 1982; Press *et al.*,

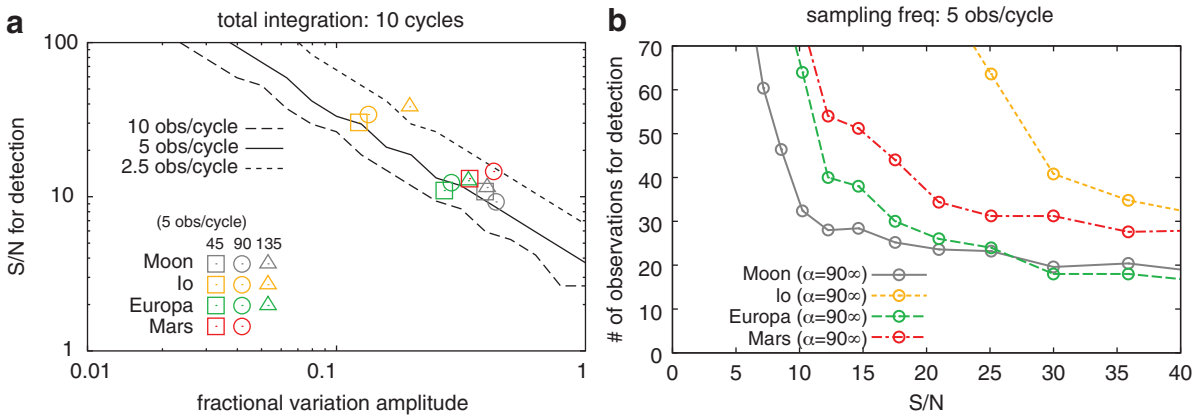

FIG. 8. (**a**) Signal-to-noise ratio (S/N) necessary to detect the periodicity of the simulated light curves of the terrestrial Moon at 1000 nm (gray), Io at 559 nm (orange), Europa at 551 nm (green), and Mars at 300–2900 nm (red) at three phase angles: $\alpha = 45°$ (square), 90° (circle), and 135° (triangle). Fifty observations randomly scattered over 10 cycles are assumed. For reference, the S/N to detect the periodicity of sinusoids with varying amplitude and varying sampling frequency (10 obs/cycle: long-dashed, 5 obs/cycle: solid, and 2.5 obs/cycle: short-dashed) are overlaid. (**b**) Number of observations needed to detect the periodicity with given S/N per observation. The terrestrial Moon at 1000 nm (gray solid), Io at 559 nm (orange short-dashed), Europa at 551 nm (green long-dashed), and Mars at 300–2900 nm (red dot-dashed) located at $\alpha = 90°$ are considered. Assumed observation frequency is 5 observations per cycle on average. Color images available online at www.liebertonline.com/ast

2007) on each mock data set and discern whether the peak of the power spectrum is present within $P_{\rm spin} \pm 0.1 P_{\rm spin}$. If the peak is present, the false-alarm probability (FAP) of the peak is computed in a randomization scheme (*e.g.*, Murdoch *et al.*, 1993). Namely, we create 1000 realizations by randomly rearranging the data points, while retaining the time spacing of observation, and perform the same periodogram analysis on them; the fraction of the realizations whose highest power exceeds the peak of the original mock data is regarded as FAP. The S/N that achieves FAP < 0.1% is claimed as successful periodicity detection. To suppress the effect of randomness of the Gaussian noise, 100 sets of mock data are created for each S/N level. The smallest S/N with which the periodicity is successfully detected for all the 100 mock data sets is recorded as the S/N necessary for periodicity measurement.

The above-mentioned procedure is performed on the simulated light curves of the Moon (1000 nm), Mercury (1000 nm), Io (559 nm), Europa (based on the grayscale map but compatible with 551 nm observation), and Mars (300–2900 nm) at three phase angles: $\alpha = 45°$, 90°, and 135°; we exclude Ganymede and Callisto from this analysis because of the insufficient matching between the simulation and the observed data (Fig. 5).

Panel (a) of Fig. 8 depicts the S/Ns necessary for periodicity measurement of the Moon, Io, Europa, and Mars when we assume 50 observations randomly scattered over 10 cycles (*i.e.*, 5 data points per cycle on average) in a plane of S/N and fractional peak-to-trough variation amplitude. The results of different phase angles are represented by three different symbols (see caption). Overlaid black lines are the results of the same analysis on sinusoids: $1 + \frac{A}{2}\cos(2\pi \cdot \frac{t}{P_{\rm spin}})$ (A is the peak-to-trough amplitude, $P_{\rm spin}$ is the spin rotation period, and t is the time) as a ruler, with varying amplitude A and varying sampling frequency (100 observations, 50 observations, 25 observations scattered over 10 cycles).

According to our estimation, in most cases, the periodicity may be safely determined with 50 data points if observational noises per data point are 3–4 times smaller than the fractional variation amplitude. With S/N $\sim$ 10, the periodicity of relatively variable targets such as the Moon, Europa, and Mars is detectable after 50 observations. For Io at 559 nm, whose fraction variation amplitude is $\sim$0.1, S/N $\sim$ 30 would be required.

To show this from a different angle, panel (b) of Fig. 8 presents the number of observations needed for periodicity detection with given S/N level, assuming that sampling frequency corresponds to 5 data points per cycle on average. Observations with S/N $\sim$ 10 and 20 may identify periodicity after $\sim$50 and $\sim$30 observations, respectively, if the target is variable with fractional amplitude 0.3–0.4, like the Moon, Europa, and Mars.

Precisely speaking, spin period measurements are affected by the phase angle. At larger phase angles, local features are traced more sharply because the illuminated and visible area is narrow. As a result, the variation amplitudes of the light curves tend to become larger, and smaller-scale fluctuations start to appear on the light curves. The former helps the determination of the spin rotation period, while the latter could disturb it by accumulating the power at higher-order periodicity (*e.g.*, $t = P_{\rm spin}$, $\frac{1}{3}P_{\rm spin}$) instead of the exact spin rotation period ($t = P_{\rm spin}$). This is the case for Io and Mars, where larger S/N is required to locate the correct periodicity at larger phase angles. For Mercury and Mars at $\alpha = 135°$, the peak at $t = \frac{1}{2}P_{\rm spin}$ tends to be stronger than the one at $t = P_{\rm spin}$ because of the double-peaked light curves (Figs. 4 and 6), and results are not displayed in Fig. 8, although half period ($t = \frac{1}{2}P_{\rm spin}$) may be detected with S/N $\sim$ 20. In reality, observations of exoplanets at large phase angles with high S/N will be challenging because of the much fainter planetary signal. For instance, a planet at $\alpha = 135°$ is 0.15 times as bright as that at $\alpha = 90°$ assuming a

Lambert sphere. This being taken into account, it will be more feasible to search for periodicity of exoplanets at smaller phase angle.

5. Discussion

5.1. Effects of atmosphere

The aim of the present study was to lay the groundwork for future characterization of the surfaces of solid exoplanets through direct imaging observations. While we considered bodies smaller than Earth with minor atmospheres, the early-stage targets of future investigations are likely to be larger planets, which tend to have atmospheres. In this section, we discuss the effects of atmospheres.

In general, the presence of an atmosphere weakens the spectral signatures of the surface. In particular, a global cover of clouds or hazes (as on Venus and Titan) would drastically modify the photometric and spectroscopic signatures of the planets by efficiently scattering back the incident light well above the surface (Fujii *et al.*, 2011). In the case of Earth, the observed multiband photometry of Earth (with patchy cloud cover) shows $\sim$20% fluctuation (Livengood *et al.*, 2011), while the cloudless Earth would produce $\sim$100% peak-to-trough variation in one spin rotation in the 700–800 nm band, due to the heterogeneous surface compositions (Ford *et al.*, 2001).

In addition, atmospheric molecules affect the spectra through molecular absorption bands and overall Rayleigh scattering. The signatures of the surface may be seen most easily at longer wavelengths (where the effects of Rayleigh scattering are smaller) through atmospheric windows, if the effects of clouds and hazes are not significant.

Obviously, the diversity of rocky/icy exoplanet surface environments will be greater than presently expected, and future targets may or may not have atmospheres. In that sense, photometric variability associated with surface geology will be worth looking for, and such signatures would potentially work in synergy with the spectroscopic information of the atmosphere for constraining the surface environment as a whole.

5.2. Other minor bodies in the Solar System

Among the atmosphereless bodies in the Solar System we did not examine in this study, an intriguing example in terms of albedo features would be Iapetus, Saturn's third-largest Moon in a synchronous orbit. One of the remarkable characteristics of Iapetus is an albedo dichotomy between the leading and trailing hemispheres: the geometric albedos of the bright and dark regions are 0.4 and 0.04, respectively (Buratti *et al.*, 2005). One of the suggested origins of the global albedo dichotomy is that the dark materials were ejected from other satellites, possibly the outer moon Phoebe (*e.g.*, Bell *et al.*, 1985; Thomas and Veverka, 1985; Verbiscer *et al.*, 2009), spread into Iapetus's orbit, and precipitated onto the leading hemisphere. The sublimation of H_2O ice would drastically change the distribution of the surface albedo and create the current shape of the dark region (Spencer and Denk, 2010; Kimura *et al.*, 2011). The huge albedo asymmetry of Iapetus roughly corresponds to a 160% peak-to-trough amplitude, which enables easier determination of the rotational period with S/N $\sim$ 5 after $\sim$15 observations if it were an exoplanet. It is also likely that such a body ''disappears'' periodically, as was the case when Iapetus was first discovered by Cassini (Van Helden, 1984). Such a peculiar feature might be possible for synchronously rotating bodies, depending on the surrounding environment.

5.3. Degeneracy in estimating surface materials

The variety of processes that alter surface reflection spectra suggests a high degree of degeneracy in possible surface conditions inferred from particular observed features. For instance, the albedo contrast of Earth in the ''red'' part of the spectrum primarily comes from the color difference of the continents and ocean, which is not the case for Mars. Then, the identification of continents/ocean should involve other diagnostics, such as the ocean's glint (*e.g.*, Williams and Gaidos, 2008; Oakley and Cash, 2009; Robinson *et al.*, 2010, 2014) or the spectroscopy of atmosphere/surface compositions (*e.g.*, Fujii *et al.*, 2013). It is likely a formidable task to uniquely determine the surface condition from one type of

Table 3. Major Geological Processes That Vary Planetary Color Regionally

Process	*Condition*	*Effect*	*Example*
Igneous activities (volcanism)	internal heat	regional cover with volcanism-related materials	Io, terrestrial Moon
Grained materials produced through weathering	atmosphere	brightening[1]	Mars
Asymmetric interaction with surrounding plasmas/materials	tidal lock and surrounding high-density plasmas/materials	hemispheric asymmetry in color	Europa, Ganymede, (Callisto)
Space weathering	(no/thin atmosphere)	reddening, darkening	terrestrial Moon, Mercury, Galilean moons
Impact excavation	(no/thin atmosphere)	regional cover with ejecta deposits (many isotropic impacts could homogenize the surface)	Mercury, Ganymede, Callisto, (terrestrial Moon)
Tectonic deformation	internal heat	brightening	(Ganymede)

[1]Effects depend on the detailed properties of the soil.

observation, and it will be important to consider multiple diagnostics available.

6. Summary

In this study, we quantitatively examined the photometric properties of the terrestrial Moon, Mercury, the Galilean moons, and Mars, with a focus on time variability due to spin rotation, as a basis for future exoplanet study. We simulated multiband light curves for each body based on recent reflectance map products as well as compiled the observed data, and interpreted the observable features through the geological characteristics of each body.

Based on the overview of the current geological insights into these bodies, we pointed out several processes that can vary the disk-averaged colors, including compositional heterogeneity due to igneous activity (on the terrestrial Moon, Mercury, and Io), diversity in particle size (on Mars), interaction between icy surfaces and surrounding materials (on Europa, Ganymede, and Callisto), and global tectonic deformation (on Ganymede). These albedo traits produce rotational light curves in the UV/visible/NIR with fractional peak-to-trough variation amplitudes widely spread in the range of 5–50%. Highly variable targets may imply that the body has, or has had, major geological activity. The wavelength dependence of the variability as well as the averaged spectra are useful for clarifying the origins. The major geological processes and their effects on the disk-averaged spectra are summarized in Table 3.

If they were exoplanets, the rotational periods would in principle be observable through periodogram analysis of the light curves, depending on the S/N and the number of observations. Signal-to-noise ratio (S/N) $\sim$ 10 per data points would allow us to detect spin rotational periods of the terrestrial Moon, Europa, and Mars after 50 observations, while S/N $\sim$ 30 is needed for Io at 559 nm.

Surveying the geological characteristics and disk-averaged photometric properties of known planets and moons illustrates realistic possibilities for investigating the surface environments of general solid exoplanets. The results presented here will also serve as a basic reference to compare the known bodies with exoplanets once comparable data become available, which would be one of the approaches to determine the uniqueness or universality of Solar System bodies.

Acknowledgments

We gratefully acknowledge discussions with Hiroki Harakawa and Bun'ei Sato on the periodogram analysis. We also appreciate the kind support from Timothy A. Livengood and Tomohiro Usui in obtaining data sets. We are thankful to David S. Spiegel and Edwin L. Turner for helpful discussions. Insightful comments from Nicolas B. Cowan and Mark Claire significantly improved this paper. The work of Y.F. is supported from the Grant-in-Aid No. 25887024 by the Japan Society for the Promotion of Science. The authors would like to thank Enago (www.enago.jp) for the English language review.

Author Disclosure Statement

No competing financial interests exist.

Abbreviations

BRDF, bidirectional reflectance distribution function; EPOCh, Extrasolar Planet Observation and Characterization; FAP, false-alarm probability; MGS, Mars Global Surveyor; MT75, Millis and Thompson (1975); NIR, near IR; S/N, signal-to-noise ratio; SSI, Solid-State Imaging; TES, Thermal Emission Spectrometer.

References

Adams, J.B. and Filice, A.L. (1967) Spectral reflectance 0.4 to 2.0 microns of silicate rock powders. *J Geophys Res* 72:5705–5715.

Arnold, L., Gillet, S., Lardière, O., Riaud, P., and Schneider, J. (2002) A test for the search for life on extrasolar planets. Looking for the terrestrial vegetation signature in the Earthshine spectrum. *Astron Astrophys* 392:231–237.

Arvidson, R., Drozd, R.J., Hohenberg, C.M., Morgan, C.J., and Poupeau, G. (1975) Horizontal transport of the regolith, modification of features, and erosion rates on the lunar surface. *The Moon* 13:67–79.

Baker, V.R., Strom, R.G., Gulick, V.C., Kargel, J.S., Komatsu, G., and Kale, V.S. (1991) Ancient oceans, ice sheets and the hydrological cycle on Mars. *Nature* 352:589–594.

Baker, V.R., Maruyama, S., and Dohm, J.M. (2007) Tharsis superplume and the geological evolution of early Mars. In *Superplumes: Beyond Plate Tectonics,* edited by D.A. Yuen, S. Maruyama, S.I. Karato, and B.F. Windley, Springer, Dordrecht, the Netherlands, pp 507–523.

Becker, T. and Geissler, P.E. (2005) Galileo global color mosaics of Io [abstract 1862]. In *36th Lunar and Planetary Science Conference Abstracts,* Lunar and Planetary Institute, Houston.

Becker, T., Archinal, B., Colvin, T., Davies, M., Gitlin, A., Kirk, R.L., and Weller, L. (2001) Final digital global maps of Ganymede, Europa, and Callisto [abstract 2009]. In *32nd Lunar and Planetary Science Conference Abstracts,* Lunar and Planetary Institute, Houston.

Bell, J.F., Cruikshank, D.P., and Gaffey, M.J. (1985) The composition and origin of the Iapetus dark material. *Icarus* 61:192–207.

Belton, M.J.S., Klaasen, K.P., Clary, M.C., Anderson, J.L., Anger, C.D., Carr, M.H., Chapman, C.R., Davies, M.E., Greeley, R., and Anderson, D. (1992) The Galileo Solid-State Imaging experiment. *Space Sci Rev* 60:413–455.

Blanco, C. and Catalano, S. (1974) On the photometric variations of the Saturn and Jupiter satellites. *Astron Astrophys* 33:105–111.

Buratti, B.J. (1995) Photometry and surface structure of the icy Galilean satellites. *J Geophys Res* 100:19061–19066.

Buratti, B.J., Cruikshank, D.P., Brown, R.H., Clark, R.N., Bauer, J.M., Jaumann, R., McCord, T.B., Simonelli, D.P., Hibbitts, C.A., Hansen, G.B., Owen, T.C., Baines, K.H., Bellucci, G., Bibring, J.P., Capaccioni, F., Cerroni, P., Coradini, A., Drossart, P., Formisano, V., Langevin, Y., Matson, D.L., Mennella, V., Nelson, R.M., Nicholson, P.D., Sicardy, B., Sotin, C., Roush, T.L., Soderlund, K., and Muradyan, A. (2005) Cassini Visual and Infrared Mapping Spectrometer observations of Iapetus: detection of CO_2. *Astrophys J* 622:L149–L152.

Cadogan, P.H. (1981) *The Moon: Our Sister Planet,* Cambridge University Press, Cambridge, UK.

Carlson, R.W., Anderson, M.S., Johnson, R.E., Schulman, M.B., and Yavrouian, A.H. (2002) Sulfuric acid production on Europa: The radiolysis of sulfur in water ice. *Icarus* 157: 456–463.

Carlson, R.W., Kargel, J.S., Douté, S., Soderblom, L.A., and Dalton, J.B. (2007) Io's surface composition. In *Io after Galileo: A New View of Jupiter's Volcanic Moon,* edited by R.M.C. Lopes and J.R. Spencer, Springer, New York, pp 193–230.

Carr, M.H. and Head, J.W. (2010) Geologic history of Mars. *Earth Planet Sci Lett* 294:185–203.

Christensen, P.R., Bandfield, J.L., Hamilton, V.E., Ruff, S.W., Kieffer, H.H., Titus, T.N., Malin, M.C., Morris, R.V., Lane, M.D., Clark, R.L., Jakosky, B.M., Mellon, M.T., Pearl, J.C., Conrath, B.J., Smith, M.D., Clancy, R.T., Kuzmin, R.O., Roush, T., Mehall, G.L., Gorelick, N., Bender, K., Murray, K., Dason, S., Greene, E., Silverman, S., and Greenfield, M. (2001) Mars Global Surveyor Thermal Emission Spectrometer experiment: investigation description and surface science results. *J Geophys Res* 106:23823–23872.

Clark, R.N. (1980) Ganymede, Europa, Callisto, and Saturn's rings—compositional analysis from reflectance spectroscopy. *Icarus* 44:388–409.

Clark, R.N. (1999) Spectroscopy of rocks and minerals, and principles of spectroscopy. In *Remote Sensing for the Earth Sciences,* edited by A.N. Rencz, Wiley, New York, pp 3–58.

Cowan, N.B. and Agol, E. (2008) Inverting phase functions to map exoplanets. *Astrophys J* 678:L129–L132.

Cowan, N.B. and Strait, T.E. (2013) Determining reflectance spectra of surfaces and clouds on exoplanets. *Astrophys J* 765:L17.

Cowan, N.B., Agol, E., Meadows, V.S., Robinson, T., Livengood, T.A., Deming, D., Lisse, C.M., A'Hearn, M.F., Wellnitz, D.D., Seager, S., Charbonneau, D., and the EPOXI Team. (2009) Alien maps of an ocean-bearing world. *Astrophys J* 700:915–923.

Cowan, N.B., Robinson, T., Livengood, T.A., Deming, D., Agol, E., A'Hearn, M.F., Charbonneau, D., Lisse, C.M., Meadows, V.S., Seager, S., Shields, A.L., and Wellnitz, D.D. (2011) Rotational variability of Earth's polar regions: implications for detecting snowball planets. *Astrophys J* 731, doi:10.1088/0004-637X/731/1/76.

Crow, C.A., McFadden, L.A., Robinson, T., Meadows, V.S., Livengood, T.A., Hewagama, T., Barry, R.K., Deming, L.D., Lisse, C.M., and Wellnitz, D. (2011) Views from EPOXI: colors in our Solar System as an analog for extrasolar planets. *Astrophys J* 729, doi:10.1088/0004-637X/729/2/130.

Des Marais, D.J., Harwit, M.O., Jucks, K.W., Kasting, J.F., Lin, D.N.C., Lunine, J.I., Schneider, J., Seager, S., Traub, W.A., and Woolf, N.J. (2002) Remote sensing of planetary properties and biosignatures on extrasolar terrestrial planets. *Astrobiology* 2:153–181.

Dohm, J.M., Maruyama, S., Baker, V.R., and Anderson, R.C. (2007) Traits and evolution of the Tharsis superplume. In *Superplumes: Beyond Plate Tectonics,* edited by D.A. Yuen, S. Maruyama, S.I. Karato, and B.F. Windley, Springer, Dordrecht, the Netherlands, pp 523–537.

Dohm, J.M., Baker, V.R., Boynton, W.V., Fairén, A.G., Ferris, J.C., Finch, M., Furfaro, R., Hare, T.M., Janes, D.M., Kargel, J.S., Karunatillake, S., Keller, J., Kerry, K., Kim, K.J., Komatsu, G., Mahaney, W.C., Schulze-Makuch, D., Marinangeli, L., Ori, G.G., Ruiz, J., and Wheelock, S.J. (2009) GRS evidence and the possibility of ancient oceans on Mars. *Planet Space Sci* 57:664–684.

Dohm, J.M., Miyamoto, H., Maruyama, S., Baker, V.R., Anderson, R.C., Hynek, B.M., Robbins, S.J., Ori, G., Komatsu, G., El Maarry, M.R., Soare, R.J., Mahaney, W.C., Kim, K.J., and Hare, T.M. (2013) Mars evolution. In *Mars: Evolution, Geology, and Exploration,* edited by A.G. Fairén, Nova Science Publishers, Hauppauge, NY, pp 1–33.

Domingue, D.L., Murchie, S.L., Chabot, N.L., Denevi, B.W., Vilas, F. (2011a) Mercury's spectrophotometric properties: Update from the Mercury Dual Imaging System observations during the third MESSENGER flyby. *Planet Space Sci* 59:1853–1872.

Domingue, D.L., Murchie, S.L., Denevi, B.W., Chabot, N.L., Blewett, D.T., Laslo, N.R., Vaughan, R.M., Kang, H.K., and Shepard, M.K. (2011b) Photometric correction of Mercury's global color mosaic. *Planet Space Sci* 59:1873–1887.

Ford, E.B., Seager, S., and Turner, E.L. (2001) Characterization of extrasolar terrestrial planets from diurnal photometric variability. *Nature* 412:885–887.

Fujii, Y. and Kawahara, H. (2012) Mapping Earth analogs from photometric variability: spin-orbit tomography for planets in inclined orbits. *Astrophys J* 755, doi:10.1088/0004-637X/755/2/101.

Fujii, Y., Kawahara, H., Suto, Y., Taruya, A., Fukuda, S., Nakajima, T., and Turner, E.L. (2010) Colors of a second Earth: estimating the fractional areas of ocean, land, and vegetation of Earth-like exoplanets. *Astrophys J* 715, doi:10.1088/0004-637X/715/2/866.

Fujii, Y., Kawahara, H., Suto, Y., Fukuda, S., Nakajima, T., Livengood, T.A., and Turner, E.L. (2011) Colors of a second Earth II. Effects of clouds on photometric characterization of Earth-like exoplanets. *Astrophys J* 738, doi:10.1088/0004-637X/738/2/184.

Fujii, Y., Turner, E.L., and Suto, Y. (2013) Variability of water and oxygen absorption bands in the disk-integrated spectra of Earth. *Astrophys J* 765, doi:10.1088/0004-637X/765/2/76.

Geissler, P.E., McEwen, A.S., Keszthelyi, L., Lopes-Gautier, R., Granahan, J., and Simonelli, D.P. (1999) Global color variations on Io. *Icarus* 140:265–282.

Hamdani, S., Arnold, L., Foellmi, C., Berthier, J., Billeres, M., Briot, D., François, P., Riaud, P., and Schneider, J. (2006) Biomarkers in disk-averaged near-UV to near-IR Earth spectra using Earthshine observations. *Astron Astrophys* 460: 617–624.

Hapke, B. (1986) Bidirectional reflectance spectroscopy. IV - The extinction coefficient and the opposition effect. *Icarus* 67:264–280.

Harris, D.L. (1961) Photometry and colorimetry of planets and satellites. In *Planets and Satellites,* edited by G.P. Kuiper and B.M. Middlehurst, The University of Chicago Press, Chicago, pp 272–342.

Hawkins, S.E., Boldt, J.D., Darlington, E.H., Espiritu, R., Gold, R.E., Gotwols, B., Grey, M.P., Hash, C.D., Hayes, J.R., Jaskulek, S.E., Kardian, C.J., Keller, M.R., Malaret, E.R., Murchie, S.L., Murphy, P.K., Peacock, K., Prockter, L.M., Reiter, R.A., Robinson, M.S., Schaefer, E.D., Shelton, R.G., Sterner, R.E., Taylor, H.W., Watters, T.R., and Williams, B.D. (2007) The Mercury Dual Imaging System on the MESSENGER spacecraft. *Space Sci Rev* 131:247–338.

Head, J.W., III, Hiesinger, H., Ivanov, M.A., Kreslavsky, M.A., Pratt, S., and Thomson, B.J. (1999) Possible ancient oceans on Mars: evidence from Mars Orbiter Laser Altimeter data. *Science* 286:2134–2137.

Hiesinger, H. and Head, J.W., III. (2006) New views of lunar geosciences: an introduction and overview. In *New Views of the Moon,* edited by B.L. Jolliff, M.A. Wieczorek, C.K. Shearer, and C.R. Neal, Mineralogical Society of America, Chantilly, VA, pp 1–81.

Hu, R., Ehlmann, B.L., and Seager, S. (2012) Theoretical spectra of terrestrial exoplanet surfaces. *Astrophys J* 752, doi:10.1088/0004-637X/752/1/7.

Irvine, W.M., Simon, T., Menzel, D.H., Charon, J., Leconte, G., Griboval, P., and Young, A.T. (1968a) Multicolor photoelectric photometry of the brighter planets. II. Observations from le Houga Observatory. *Astron J* 73:251–264.

Irvine, W.M., Simon, T., Menzel, D.H., Pikoos, C., and Young, A.T. (1968b) Multicolor photoelectric photometry of the brighter planets. III. Observations from Boyden Observatory. *Astron J* 73:807.

Johnson, R.E. (1997) Note: Polar ''caps'' on Ganymede and Io revisited. *Icarus* 128:469–471.

Johnson, T.V. (1971) Galilean satellites: narrowband photometry 0.30 to 1.10 microns. *Icarus* 14:94–111.

Kaltenegger, L., Traub, W.A., and Jucks, K.W. (2007) Spectral evolution of an Earth-like planet. *Astrophys J* 658: 598–616.

Kaltenegger, L., Selsis, F., Fridlund, M., Lammer, H., Beichman, C., Danchi, W., Eiroa, C., Henning, T., Herbst, T., Léger, A., Liseau, R., Lunine, J., Paresce, F., Penny, A., Quirrenbach, A., Röttgering, H., Schneider, J., Stam, D., Tinetti, G., and White, G.J. (2010) Deciphering spectral fingerprints of habitable exoplanets. *Astrobiology* 10:89–102.

Kato, M., Sasaki, S., Tanaka, K., Iijima, Y., and Takizawa, Y. (2008) The Japanese lunar mission SELENE: science goals and present status. *Adv Space Res* 42:294–300.

Kawahara, H. and Fujii, Y. (2010) Global mapping of Earth-like exoplanets from scattered light curves. *Astrophys J* 720: 1333–1350.

Kawahara, H. and Fujii, Y. (2011) Mapping clouds and terrain of Earth-like planets from photometric variability: demonstration with planets in face-on orbits. *Astrophys J* 739:L62.

Khurana, K.K., Pappalardo, R.T., Murphy, N., and Denk, T. (2007) The origin of Ganymede's polar caps. *Icarus* 191: 193–202.

Kimura, J., Kawamura, T., Morito, H., Morota, T., Honda, C., Kuramoto, K., and Okada, T. (2011) Sublimation's impact on temporal change of albedo dichotomy on Iapetus. *Icarus* 214:596–605.

Kokubo, E. and Genda, H. (2010) Formation of terrestrial planets from protoplanets under a realistic accretion condition. *Astrophys J* 714:L21–L25.

Kokubo, E. and Ida, S. (2007) Formation of terrestrial planets from protoplanets. II. Statistics of planetary spins. *Astrophys J* 671:2082–2090.

Livengood, T.A., Deming, L.D., A'Hearn, M.F., Charbonneau, D., Hewagama, T., Lisse, C.M., McFadden, L.A., Meadows, V.S., Robinson, T.D., Seager, S., and Wellnitz, D.D. (2011) Properties of an Earth-like planet orbiting a Sun-like star: Earth observed by the EPOXI mission. *Astrobiology* 11:907–930.

Lomb, N.R. (1976) Least-squares frequency analysis of unequally spaced data. *Astrophys Space Sci* 39:447–462.

Lucey, P., Korotev, R.L., Gillis, J.J., Taylor, L.A., Lawrence, D., Campbell, B.A., Elphic, R., Feldman, B., Hood, L.L., Hunten, D., Mendillo, M., Noble, S., Papike, J.J., Reedy, R.C., Lawson, S., Prettyman, T., Gasnault, O., and Mauric, S. (2006) Understanding the lunar surface and space-moon interactions. In *New Views of the Moon,* edited by B.L. Jolliff, M.A. Wieczorek, C.K. Shearer, and C.R. Neal, Mineralogical Society of America, Chantilly, VA, pp 83–220.

Lundock, R., Ichikawa, T., Okita, H., Kurita, K., Kawabata, K.S., Uemura, M., Yamashita, T., Ohsugi, T., Sato, S., and Kino, M. (2009) Tohoku-Hiroshima-Nagoya planetary spectra library: a method for characterizing planets in the visible to near infrared. *Astron Astrophys* 507:1649–1658.

Mallama, A. (2009) Characterization of terrestrial exoplanets based on the phase curves and albedos of Mercury, Venus and Mars. *Icarus* 204:11–14.

Mallama, A., Wang, D., and Howard, R.A. (2002) Photometry of Mercury from SOHO/LASCO and Earth. The phase function from 2 to 170 deg. *Icarus* 155:253–264.

McCord, T.B., Hansen, G.B., Fanale, F.P., Carlson, R.W., Matson, D.L., Johnson, T.V., Smythe, W.D., Crowley, J.K., Martin, P.D., Ocampo, A., Hibbitts, C.A., and Granahan, J.C. (1998) Salts on Europa's surface detected by Galileo's Near Infrared Mapping Spectrometer. *Science* 280:1242–1245.

McEwen, A.S., Hansen, C.J., Delamere, W.A., Eliason, E.M., Herkenhoff, K.E., Keszthelyi, L., Gulick, V.C., Kirk, R.L., Mellon, M.T., Grant, J.A., Thomas, N., Weitz, C.M., Squyres, S.W., Bridges, N.T., Murchie, S.L., Seelos, F., Seelos, K., Okubo, C.H., Milazzo, M.P., Tornabene, L.L., Jaeger, W.L., Byrne, S., Russell, P.S., Griffes, J.L., Martínez-Alonso, S., Davatzes, A., Chuang, F.C., Thomson, B.J., Fishbaugh, K.E., Dundas, C.M., Kolb, K.J., Banks, M.E., and Wray, J.J. (2007) A closer look at water-related geologic activity on Mars. *Science* 317:1706–1709.

Millis, R.L. and Thompson, D.T. (1975) UBV photometry of the Galilean satellites. *Icarus* 26:408–419.

Moore, J.M., Chapman, C.R., Bierhans, E.B., Greeley, R., Chuang, F.C., Klemaszewski, J., Clark, R.N., Dalton, J.B., Hibbits, C.A., Schenk, P.M., Spencer, J.R., and Wagner, R. (2004) Callisto. In *Jupiter,* Cambridge University Press, Cambridge, UK, pp 397–426.

Morota, T., Haruyama, J., Ohtake, M., Matsunaga, T., Honda, C., Yokota, Y., Kimura, J., Ogawa, Y., Hirata, N., Demura, H., Iwasaki, A., Sugihara, T., Saiki, K., Nakamura, R., Kobayashi, S., Ishihara, Y., Takeda, H., and Hiesinger, H. (2011) Timing and characteristics of the latest mare eruption on the Moon. *Earth Planet Sci Lett* 302:255–266.

Morris, R.V., Golden, D.C., Bell, J.F., III, Shelfer, T.D., Scheinost, A.C., Hinman, N.W., Furniss, G., Mertzman, S.A., Bishop, J.L., Ming, D.W., Allen, C.C., and Britt, D.T. (2000) Mineralogy, composition, and alteration of Mars Pathfinder rocks and soils: evidence from multispectral, elemental, and magnetic data on terrestrial analogue, SNC meteorite, and Pathfinder samples. *J Geophys Res* 105:1757–1817.

Morris, R.V., Golden, D.C., Ming, D.W., Shelfer, T.D., Jorgensen, L.C., Bell, J.F., III, Graff, T.G., and Mertzman, S.A. (2001) Phyllosilicate-poor palagonitic dust from Mauna Kea Volcano (Hawaii): a mineralogical analogue for magnetic martian dust? *J Geophys Res* 106:5057–5083.

Morrison, D. and Morrison, N.D. (1977) Photometry of the Gallilean satellites. In *Planetary Satellites,* edited by J.A. Burns, University of Arizona Press, Tucson, pp 363–378.

Morrison, D., Morrison, N.D., and Lazarewicz, A.R. (1974) Four-color photometry of the Galilean satellites. *Icarus* 23:399–416.

Murdoch, K.A., Hearnshaw, J.B., and Clark, M. (1993) A search for substellar companions to southern solar-type stars. *Astrophys J* 413:349–363.

Nakamura, R., Yamamoto, S., Matsunaga, T., Ishihara, Y., Morota, T., Hiroi, T., Takeda, H., Ogawa, Y., Yokota, Y., Hirata, N., Ohtake, M., and Saiki, K. (2012) Compositional evidence for an impact origin of the Moon's Procellarum basin. *Nat Geosci* 5:775–778.

Nash, D.B. and Johnson, T.V. (1979) Albedo distribution on Io's surface. *Icarus* 38:69–74.

Nittler, L.R., Starr, R.D., Weider, S.Z., McCoy, T.J., Boynton, W.V., Ebel, D.S., Ernst, C.M., Evans, L.G., Goldsten, J.O.,

Hamara, D.K., Lawrence, D.J., McNutt, R.L., Schlemm, C.E., Solomon, S.C., and Sprague, A.L. (2011) The major-element composition of Mercury's surface from MESSENGER X-ray spectrometry. *Science* 333:1847–1850.

Oakley, P.H.H. and Cash, W. (2009) Construction of an Earth model: analysis of exoplanet light curves and mapping the next Earth with the New Worlds Observer. *Astrophys J* 700:1428–1439.

Pallé, E., Ford, E.B., Seager, S., Montañés-Rodríguez, P., and Vazquez, M. (2008) Identifying the rotation rate and the presence of dynamic weather on extrasolar Earth-like planets from photometric observations. *Astrophys J* 676:1319–1329.

Pappalardo, R.T., Head, J.W., Greeley, R., Sullivan, R.J., Pilcher, C., Schubert, G., Moore, W.B., Carr, M.H., Moore, J.M., Belton, M.J.S., and Goldsby, D.L. (1998) Geological evidence for solid-state convection in Europa's ice shell. *Nature* 391:365–368.

Porco, C.C., Helfenstein, P., Thomas, P.C., Ingersoll, A.P., Wisdom, J., West, R., Neukum, G., Denk, T., Wagner, R., Roatsch, T., Kieffer, S., Turtle, E., McEwen, A., Johnson, T.V., Rathbun, J., Veverka, J., Wilson, D., Perry, J., Spitale, J., Brahic, A., Burns, J.A., Del Genio, A.D., Dones, L., Murray, C.D., and Squyres, S. (2006) Cassini observes the active south pole of Enceladus. *Science* 311:1393–1401.

Press, W.H., Teukolsky, S.A., Vetterling, W.T., and Flannery, B.P. (2007) *Numerical Recipes: The Art of Scientific Computing,* 3rd ed., Cambridge University Press, New York.

Qiu, J., Goode, P.R., Pallé, E., Yurchyshyn, V., Hickey, J., Montañés-Rodriguez, P., Chu, M.C., Kolbe, E., Brown, C.T., and Koonin, S.E. (2003) Earthshine and the Earth's albedo: 1. Earthshine observations and measurements of the lunar phase function for accurate measurements of the Earth's Bond albedo. *J Geophys Res Atmospheres* 108, doi:10.1029/2003JD003610.

Rhodes, E.A., Evans, L.G., Nittler, L.R., Starr, R.D., Sprague, A.L., Lawrence, D.J., McCoy, T.J., Stockstill-Cahill, K.R., Goldsten, J.O., Peplowski, P.N., Hamara, D.K., Boynton, W.V., and Solomon, S.C. (2011) Analysis of MESSENGER Gamma-Ray Spectrometer data from the Mercury flybys. *Planet Space Sci* 59:1829–1841.

Robinson, T.D. (2011) Modeling the infrared spectrum of the Earth-Moon system: implications for the detection and characterization of Earthlike extrasolar planets and their Moonlike companions. *Astrophys J* 741, doi:10.1088/0004-637X/741/1/51.

Robinson, T.D., Meadows, V.S., and Crisp, D. (2010) Detecting oceans on extrasolar planets using the glint effect. *Astrophys J* 721:L67–L71.

Robinson, T.D., Meadows, V.S., Crisp, D., Deming, D., A'Hearn, M.F., Charbonneau, D., Livengood, T.A., Seager, S., Barry, R.K., Hearty, T., Hewagama, T., Lisse, C.M., McFadden, L.A., and Wellnitz, D.D. (2011) Earth as an extrasolar planet: Earth model validation using EPOXI Earth observations. *Astrobiology* 11:393–408.

Robinson, T.D., Ennico, K., Meadows, V.S., Sparks, W., Bussey, D., Ben J., Schwieterman, E.W., and Breiner, J. (2014) Detection of ocean glint and ozone absorption using LCROSS Earth observations. *Astrophys J* 787, doi:10.1088/0004-637X/787/2/171.

Ruff, S.W. and Christensen, P.R. (2002) Bright and dark regions on Mars: particle size and mineralogical characteristics based on Thermal Emission Spectrometer data. *J Geophys Res* 107, doi:10.1029/2001JE001580.

Sanromá, E. and Pallé, E. (2012) Reconstructing the photometric light curves of Earth as a planet along its history. *Astrophys J* 744, doi:10.1088/0004-637X/744/2/188.

Sanromá, E., Pallé, E., and García Muñoz, A. (2013) On the effects of the evolution of microbial mats and land plants on the Earth as a planet. Photometric and spectroscopic light curves of paleo-Earths. *Astrophys J* 766, doi:10.1088/0004-637X/766/2/133.

Scargle, J.D. (1982) Studies in astronomical time series analysis. II—Statistical aspects of spectral analysis of unevenly spaced data. *Astrophys J* 263:835–853.

Schaaf, C.B., Gao, F., Strahler, A.H., Lucht, W., Li, X., Tsang, T., Strugnell, N.C., Zhange, X., Jin, Y., Muller, J.P., Lewis, P., Barnsley, M., Hobson, P., Disney, M., Roberts, G., Dunderdale, M., Doll, C., d'Entremont, R.P., Hu, B., Liang, S., Privett, J.L., and Roy, D. (2002) First operational BRDF, albedo nadir reflectance products from MODIS. *Remote Sens Environ* 83:135–148.

Schenk, P.M., Chapman, C.R., Zahnle, K., and Moore, J.M., (2004) Ages and interiors: the cratering record of the Galilean satellites. In *Jupiter,* Cambridge University Press, Cambridge, UK, pp 427–456.

Schultz, P.H. (1989) Cratering on Mercury: a relook. In *Mercury,* edited by F. Vilas, C.R. Chapman, and M.S. Matthews, University of Arizona Press, Tucson, pp 274–335.

Showman, A.P., Stevenson, D.J., and Malhotra, R. (1997) Coupled orbital and thermal evolution of Ganymede. *Icarus* 129:367–383.

Spencer, J.R. and Denk, T. (2010) Formation of Iapetus extreme albedo dichotomy by exogenically triggered thermal ice migration. *Science* 327:432–435.

Squyres, S.W., Arvidson, R.E., Bell, J.F., Calef, F., Clark, B.C., Cohen, B.A., Crumpler, L.A., de Souza, P.A., Farrand, W.H., Gellert, R., Grant, J., Herkenhoff, K.E., Hurowitz, J.A., Johnson, J.R., Jolliff, B.L., Knoll, A.H., Li, R., McLennan, S.M., Ming, D.W., Mittlefehldt, D.W., Parker, T.J., Paulsen, G., Rice, M.S., Ruff, S.W., Schröder, C., Yen, A.S., and Zacny, K. (2012) Ancient impact and aqueous processes at Endeavour Crater, Mars. *Science* 336:570–576.

Stebbins, J. and Jacobsen, T.S. (1928) Further photometric measures of Jupiter's satellites and Uranus, with tests of the solar constant. *Lick Observatory Bulletin* 13:180–195.

Strom, R.G. (1979) Mercury—a post-Mariner 10 assessment. *Space Sci Rev* 24:3–70.

Taylor, S.R. (1982) *Planetary Science: A Lunar Perspective,* Lunar and Planetary Institute, Houston.

Thomas, P. and Veverka, J. (1985) Hyperion—analysis of Voyager observations. *Icarus* 64:414–424.

Tinetti, G., Meadows, V.S., Crisp, D., Fong, W., Fishbein, E., Turnbull, M., and Bibring, J. (2006a) Detectability of planetary characteristics in disk-averaged spectra. I: The Earth model. *Astrobiology* 6:34–47.

Tinetti, G., Meadows, V.S., Crisp, D., Kiang, N.Y., Kahn, B.H., Fishbein, E., Velusamy, T., and Turnbull, M. (2006b) Detectability of planetary characteristics in disk-averaged spectra. II: Synthetic spectra and light-curves of Earth. *Astrobiology* 6:881–900.

Traub, W.A. (2003) Extrasolar planet characteristics in the visible wavelength range. In *Towards Other Earths: DARWIN/TPF and the Search for Extrasolar Terrestrial Planets: Proceedings,* ESA SP-539, edited by M. Fridlund, T. Henning, and H. Lacoste, ESA Publications Division, Noordwijk, the Netherlands, pp 231–239.

Turnbull, M.C., Traub, W.A., Jucks, K.W., Woolf, N.J., Meyer, M.R., Gorlova, N., Skrutskie, M.F., and Wilson, J.C. (2006) Spectrum of a habitable world: Earthshine in the near-infrared. *Astrophys J* 644:551–559.

Van Helden, A. (1984) Saturn through the telescope: a brief historical survey. In *Saturn,* edited by T. Gehrels and M.S. Matthews, University of Arizona Press, Tucson, 23–43.

Verbiscer, A.J., Skrutskie, M.F., and Hamilton, D.P. (2009) Saturn's largest ring. *Nature* 461:1098–1100.

Warren, P.H. (1990) Lunar anorthosites and the magma-ocean plagioclase-flotation hypotheses: importance of FeO enrichment in the parent magma. *Am Mineral* 75:46–58.

Whitaker, E.A. (1981) The lunar Procellarum basin. In *Multi-Ring Basins: Formation and Evolution,* edited by R.B. Merill and P.H. Schultz, Pergamon Press, New York, pp 105–111.

Wilhelms, D.E., McCauley, J.F., and Trask, N.J. (1987) *The Geologic History of the Moon,* U.S. Geological Survey, Denver, CO.

Williams, D.M. and Gaidos, E. (2008) Detecting the glint of starlight on the oceans of distant planets. *Icarus* 195:927–937.

Woolf, N.J., Smith, P.S., Traub, W.A., and Jucks, K.W. (2002) The spectrum of Earthshine: a pale blue dot observed from the ground. *Astrophys J* 574:430–433.

Yokota, Y., Matsunaga, T., Ohtake, M., Haruyama, J., Nakamura, R., Yamamoto, S., Ogawa, Y., Morota, T., Honda, C., Saiki, K., Nagasawa, K., Kitazato, K., Sasaki, S., Iwasaki, A., Demura, H., Hirata, N., Hiroi, T., Honda, R., Iijima, Y., and Mizutani, H. (2011) Lunar photometric properties at wavelengths 0.5–1.6 μm acquired by SELENE spectral profiler and their dependency on local albedo and latitudinal zones. *Icarus* 215:639–660.

Young, A.T. and Irvine, W.M. (1967) Multicolor photoelectric photometry of the brighter planets. I. Program and procedure. *Astron J* 72:945.

Zahnle, K., Schenk, P., Levison, H., and Dones, L. (2003) Cratering rates in the outer Solar System. *Icarus* 163:263–289.

Address correspondence to:
Yuka Fujii
Earth-Life Science Institute
Tokyo Institute of Technology
2-12-1-IE-28
Ookayama
Meguro-ku
Tokyo
152-8550
Japan

E-mail: yuka.fujii@elsi.jp

Submitted 6 March 2014
Accepted 19 July 2014